

Quantum interference in graphene nanoconstrictions

Pascal Gehring, Hatef Sadeghi, Sara Sangtarash, Chit Siong Lau, Junjie Liu, Arzhang Ardavan, Jamie H. Warner, Colin J. Lambert, G. Andrew D. Briggs, and Jan A. Mol

Nano Lett., **Just Accepted Manuscript** • DOI: 10.1021/acs.nanolett.6b01104 • Publication Date (Web): 13 Jun 2016

Downloaded from <http://pubs.acs.org> on June 14, 2016

Just Accepted

“Just Accepted” manuscripts have been peer-reviewed and accepted for publication. They are posted online prior to technical editing, formatting for publication and author proofing. The American Chemical Society provides “Just Accepted” as a free service to the research community to expedite the dissemination of scientific material as soon as possible after acceptance. “Just Accepted” manuscripts appear in full in PDF format accompanied by an HTML abstract. “Just Accepted” manuscripts have been fully peer reviewed, but should not be considered the official version of record. They are accessible to all readers and citable by the Digital Object Identifier (DOI®). “Just Accepted” is an optional service offered to authors. Therefore, the “Just Accepted” Web site may not include all articles that will be published in the journal. After a manuscript is technically edited and formatted, it will be removed from the “Just Accepted” Web site and published as an ASAP article. Note that technical editing may introduce minor changes to the manuscript text and/or graphics which could affect content, and all legal disclaimers and ethical guidelines that apply to the journal pertain. ACS cannot be held responsible for errors or consequences arising from the use of information contained in these “Just Accepted” manuscripts.



Quantum interference in graphene nanoconstrictions

Pascal Gehring^{1,*}, Hatef Sadeghi², Sara Sangtarash², Chit Siong Lau¹, Junjie Liu¹, Arzhang Ardavan³,
Jamie H. Warner¹, Colin J. Lambert², G. Andrew. D. Briggs¹, Jan A. Mol¹

¹*Department of Materials, University of Oxford, 16 Parks Road, Oxford OX1 3PH, United Kingdom*

²*Quantum Technology Centre, Physics Department, Lancaster University, Lancaster LA1 4YB, United Kingdom*

³*Clarendon Laboratory, Department of Physics, University of Oxford, Parks Road, Oxford OX1 3PU, United Kingdom*

*pascal.gehring@materials.ox.ac.uk

Abstract

We report quantum interference effects in the electrical conductance of chemical vapour deposited graphene nanoconstrictions fabricated using feedback controlled electroburning. The observed multi-mode Fabry-Pérot interferences can be attributed to reflections at potential steps inside the channel. Sharp anti-resonance features with a Fano line shape are observed. Theoretical modelling reveals that these Fano resonances are due to localised states inside the constriction, which couple to the delocalised states that also give rise to the Fabry-Pérot interference patterns. This study provides new insight into the interplay between two fundamental forms of quantum interference in graphene nanoconstrictions.

KEYWORDS: graphene, quantum interference, Fano resonance, break junction, Fabry-Pérot

A key feature of electron transport through single molecules and phase-coherent nanostructures is the appearance of transport resonances associated with quantum interference.¹ Examples include Breit-Wigner resonances, multi-path Fabry-Pérot resonances and Fano resonances. Fano resonances can be observed when a localised state interacts with a continuum of extended states and can lead to very steep gradients in the transmission. Unlike Breit-Wigner resonances, they are not life-time broadened

1
2
3 by coupling to the electrodes. The steep slope of Fano resonances makes them attractive for low-
4 power switching and for creating structures with high thermoelectric performance.² In what follows,
5 we report the first observation of Fano resonances in electroburnt graphene nanoconstrictions. In
6 addition to these Fano features, the conductance maps exhibit interference patterns which we attribute
7 to multi-mode Fabry-Pérot (FP) interferences. Theoretical modelling reveals that the Fano resonances
8 arise from interaction between the delocalised state giving rise to the Fabry-Pérot pattern and a
9 localised state inside the constriction.
10

11
12
13 Carbon-based nanostructures, such as metallic or semiconducting single carbon chains^{3, 4}, graphene
14 nanoribbons and graphene nanoconstrictions are interesting platforms for the study of spintronics⁵ and
15 might enable novel technological applications⁶. Graphene nanoconstrictions and nanogaps also
16 provide a robust platform for studying the electric⁷, thermoelectric⁸ and magnetic⁹ properties of single
17 molecules. When they are sufficiently narrow, graphene nanoribbons can be used to build field-effect
18 transistors with an on/off ratio that can exceed 1000.¹⁰ In very narrow constrictions, with a width
19 smaller than the electronic wavelength of electrons, quantum interference effects in analogy to
20 subwavelength optics are predicted^{11, 12}. Graphene nanoconstrictions have been fabricated by means of
21 electron beam lithography¹³, gold break-junction etching masks¹⁰, local gating¹⁴ and electroburning of
22 graphene^{15, 16}. Electroburning has also been used to fabricate graphene quantum dots with addition
23 energies up to 1.6 eV, enabling the observation of Coulomb blockade at room temperature¹⁷. In this
24 study we use feedback-controlled electroburning to narrow down lithographically-defined bowtie
25 shaped graphene constrictions¹⁸ and study their electronic transport behaviour.
26
27

28
29
30 Our devices are fabricated from single-layer CVD-grown graphene¹⁹ which we transfer onto a
31 Si/300nm SiO₂ wafer with pre-patterned 10 nm Cr / 70 nm Au contacts. We pattern the graphene into
32 a bowtie shape (see Figure 1a,b) using standard electron beam lithography and O₂ plasma etching.
33 The channel length L of the devices and the width W of the narrowest part of the constriction are 4 μm
34 and 200 nm, respectively (see Figure 1a). Our devices are p-doped with a Dirac point V_{Dirac} around 60
35 V (see Figure 1c). The single-layer nature of the graphene constriction is confirmed by the intensity
36 ratio $I(2\text{D}) / I(\text{G}) \gg 1$ of the Raman G and 2D peaks (see Figure 1d) and the fact that the 2D peak
37
38
39
40
41
42
43
44
45
46
47
48
49
50
51
52
53
54
55
56
57
58
59
60

1
2
3 consists of a single Lorentzian.^{20, 21} In addition, we observe a D and D' peak which we attribute to the
4 defective graphene edges formed during the plasma etching.²¹ These defect peaks are not present in
5 bulk single-layer graphene samples.¹⁹ To narrow down the constriction we use a feedback-controlled
6 electroburning technique in air, similar to the one described in Ref¹⁸. We ramp-up a voltage applied
7 between the source and drain contact while monitoring the current with a 5 kHz sampling rate (see
8 Figure 1b). As soon as a drop in the current is detected, the voltage is quickly ramped back to zero.
9 This cycle is repeated until the low bias source-drain resistance of the device, which is measured after
10 each burning cycle, exceeds a threshold resistance of 500 M Ω . The feedback conditions are adjusted
11 for each burning cycle depending on the threshold voltage V_{th} at which the drop in the previous cycle
12 occurred. The current-voltage ($I - V_b$) traces of a typical electroburning process are shown in Figure
13 1e, where the $I - V_b$ traces before electroburning and after the threshold resistance is reached are
14 coloured blue and red, respectively.
15
16
17
18
19
20
21
22
23
24
25
26

27
28 During electroburning, the constriction is narrowed down and as a result the resistance of the device
29 increases. At the final stage, the (only several atoms wide) constriction can break completely and a
30 nanometre sized gap is formed.¹² However, for many devices the threshold resistance is reached
31 before a gap is fully formed. In these cases, narrow graphene constrictions or small graphene islands
32 are left between the mesoscopic graphene leads. Graphene quantum dots formed in this manner have
33 been widely studied^{15-17, 22} as a possible platform for room temperature single-electron transistors. In
34 the following we discuss the details of the transport characteristics of empty graphene nanogaps,
35 quantum dots and nanoconstrictions recorded at $T = 4$ K in vacuum ($\sim 10^{-6}$ mbar).
36
37
38
39
40
41
42
43
44

45 The transport regime which we attribute to an empty gap is characterised by low currents and $I - V_b$
46 characteristics that can be fitted using the standard Simmons model²³ for tunnelling through a single
47 trapezoidal barrier between source and drain (see Figure 2a). In addition, the $I - V_b$ characteristics
48 show no or a relatively small back gate dependence (see Figure 2b). We find gap sizes of 0.5 – 2.5 nm
49 for these junctions, making them a promising platform for single molecule electronics.^{7, 24, 25}
50
51
52
53
54
55

56 Devices in the weakly coupled quantum dot regime show suppressed current at low bias (see Figure
57 2c) and characteristic Coulomb diamonds as a function of bias and gate voltage (see Figure 2d). These
58
59
60

1
2
3 transport features are indicative of sequential electron tunnelling via a weakly coupled quantum dot
4 between source and drain.²⁶ From the size of the Coulomb diamonds we can extract addition energies
5 for these quantum dots ranging from 20 to 800 meV, comparable to those found by other groups in
6 similar systems.^{13, 15-17} The formation of graphene quantum dots during electroburning process is the
7 result of electron/hole localisation due to charge puddles and/or edge disorder as the graphene channel
8 gets narrower.²⁷ Theoretical calculations have also shown that localised states can form along the
9 edges of wedge-shaped nanoconstrictions.²⁸ Furthermore, it is possible that small graphene islands on
10 the order of several nm form, which are only weakly coupled to the graphene leads.¹⁷

11
12
13
14
15
16
17
18
19
20 The conductance maps of strongly-coupled devices are dominated by “chess board”-like interference
21 patterns as shown in Figure 2f. In some samples we could observe a transition from this chess board
22 pattern to a Coulomb diamond regime at high positive gate voltages of $\gtrsim 40$ V. This observation is
23 similar to results found in recent studies on short graphene junctions^{29, 30} and narrow graphene
24 constrictions³¹. In the latter, the chess board pattern was attributed to interference effects of extended
25 states in the source or drain graphene lead connecting the constriction.³¹ In general, interference
26 effects occur on a length scale on the order of the phase coherence length, but can have different
27 origins. If the transport in the graphene sample is diffusive, i.e. when charge carriers are
28 predominantly scattered at random impurities like edge disorder, point defects or charge puddles,²⁷ the
29 origin of the interference pattern is most likely due to quantum interferences of different random
30 scattering paths (universal conductance fluctuations, UCFs). If the channel length is on the order of or
31 shorter than the mean free path of the carriers (quasi-ballistic transport regime), reflections in the
32 channel result in quasi-periodic multi-mode or collective and periodic single-mode Fabry-Pérot
33 interferences. Carriers can get reflected at the metal contacts³⁰ or at potential barriers formed by
34 intentional local doping.³² Whether single- or multi-mode interference is observed strongly depends
35 on the detailed device geometry.³³

36
37
38
39
40
41
42
43
44
45
46
47
48
49
50
51
52
53 Fabry-Pérot interference effects have previously been observed in 1D nanowires³⁴, carbon nanotubes³⁵
54 and 2D graphene³⁰, while UCFs have been observed in mesoscopic single-³⁶, bi- and tri-layer³⁷ and
55 epitaxial graphene samples³⁸. To distinguish between these different types of quantum interference,
56
57
58
59
60

1
2
3 the chess board conductance patterns need to be carefully analysed for hidden periodicities.³⁰ From
4 the characteristic energy spacing between single features in the conductance maps and Fast Fourier
5 Transforms (FFTs) of the data shown in Figure 2f (see Figure S6a and b in the Supplementary
6 Information) we can extract a typical energy spacing of 4 – 5 meV. Using a particle-in-a-box
7 approximation³⁰ we estimate the relevant length scale $L = h v_F / (2E)$ to be between 400 nm for the
8 theoretical local density approximation limit of the Fermi velocity of $v_F = 0.8 \times 10^6$ m/s and 1.1 μm for
9 a Fermi velocity of $v_F = 2.4 \times 10^6$ m/s measured for CVD graphene on a quartz substrate.³⁹ This length
10 scale corresponds to half the minimal distance over which the electrons remain phase coherent,
11 therefore we can infer a lower bound for the phase coherence length $L_\phi > 800$ nm in our samples.²⁹
12 This value is similar to the value found for exfoliated graphene on SiO_2 ⁴⁰, epitaxial graphene⁴¹ and
13 CVD graphene⁴². For short and wide devices small incident angles dominate (longitudinal modes) and
14 resonances appear at $k_F L = n\pi$.³² However, since our devices are not in the limit $W/L \gg 1$, both
15 longitudinal and transversal modes need to be considered. To model conductance maps for different
16 aspect ratios we have performed nearest-neighbour tight-binding calculations³³ (see section S5
17 Supplementary Information). Our calculations confirm that for $W \gg L$ a periodic interference pattern
18 with high contrast can be observed. This is due to the fact that the energy of transversal modes $E_W =$
19 $h v_F / (2W)$ gets negligibly small. The same holds for the 1D limit $W \rightarrow 0$, where E_W goes to infinity. In
20 both cases the transport is dominated by longitudinal modes only. In the intermediate multi-mode
21 regime, periodic longitudinal modes can still be observed in the FFT but with much smaller contrast.
22 Since the aspect ratio W/L of our devices is close to unity we expect that the interference pattern
23 shown in Figure 2b will only be quasi-periodic because of multi-mode interferences. Moreover, the
24 fact that the width W of the samples is not constant will cause the transversal modes to become
25 chaotic.¹¹

26
27
28
29
30
31
32
33
34
35
36
37
38
39
40
41
42
43
44
45
46
47
48
49
50 Because the measured chess board pattern is only quasi-periodic, we cannot exclude UCFs as an
51 origin of the observed pattern. UCFs are normally most pronounced at low doping concentrations
52 when the electrochemical potential of graphene is close to the Dirac point.³⁰ This is unlikely to be the
53 case in our p -doped graphene junctions. In addition, the periodicity which we can correlate with the
54
55
56
57
58
59
60

1
2
3 geometry of the device is very similar for all devices investigated in this study, which makes multi-
4 mode Fabry-Pérot interferences a more likely mechanism to explain our data.
5
6

7
8 Next, we will investigate the microscopic origin of the FP reflections. Based on our assumption for
9 the Fermi velocity (see above) we estimate that carriers are coherently reflected on a length scale of \sim
10 1 μm . The visibility/intensity of FP interferences is determined by the reflectance of the potential
11 steps. Unipolar cavities have a small finesse and result in a small visibility $(G_{\text{max}} - G_{\text{min}}) / (G_{\text{max}} +$
12 $G_{\text{min}})$ since the conservation of pseudospin suppresses backscattering in graphene.³² A smooth bipolar
13 potential step like a pn junction formed near a metal-graphene contact has a much higher finesse and
14 leads to pronounced resonance pattern.³² However, since the length scale of less than 1 μm found
15 above is much smaller than the channel length of 4 μm of our devices there need to be additional
16 potential steps inside the graphene channel apart from the metal contacts. From scanning electron
17 microscopy and micro Raman spectroscopy (see Sections S1 and S4 in the Supplementary
18 Information) we can infer that the local hole concentration within a region of several hundreds of nm
19 around the graphene constriction is increased during electroburning. The increase of hole doping of
20 graphene on SiO_2 annealed in air was intensively studied and attributed to doping by O_2 and moisture
21 and a change in the degree of coupling between graphene and SiO_2 .⁴³ This increased p doping can
22 result in the formation of a pp^+p junction in the central region of the devices (see Figure S6c and d in
23 the Supplementary Information). Possible resonance conditions are reflections between the gold
24 contact/the pn junction close to the gold contact and the pp^+p junction or reflections within the pp^+p
25 junction which all have a characteristic length scale of several hundreds of nm. This length scale is on
26 the order of the-mean-free path of charge carriers in our devices (see Supplementary Information),
27 which further corroborates our interpretation that the chess board pattern arises from FP interferences
28 rather than scattering at random impurities inside the channel. The visibility of the FP interferences
29 $(G_{\text{max}} - G_{\text{min}}) / (G_{\text{max}} + G_{\text{min}}) > 10\%$ is high in our devices, which indicates that the unipolar p^+p
30 interfaces need to have a sharp potential drop with $k_{\text{F}}d \ll 1$, where d is the length over which the
31 carrier density changes.⁴⁴ We estimate this length scale by calculating the Fermi vector using $n = k_{\text{F}}^2/\pi$
32
33
34
35
36
37
38
39
40
41
42
43
44
45
46
47
48
49
50
51
52
53
54
55
56
57
58
59
60

1
2
3 and the charge carrier concentration $n = C_g^2(V_g - V_{\text{Dirac}})^2/e^2$,³⁰ where C_g is the capacitance of the
4 back gate and e is the elementary charge. For $V_{\text{Dirac}} = 60$ V (see Figure 1c), d is on the order of 3 nm.
5
6

7
8 We only see interference patterns in nearly fully-burned devices and not directly after the first
9 electroburning steps. We attribute this to the decreasing conductance of the graphene constriction
10 during electroburning, which decreases the denominator in $(G_{\text{max}} - G_{\text{min}}) / (G_{\text{max}} + G_{\text{min}})$ and thus
11 increases the visibility of the interferences. Another possible explanation for the onset of interference
12 pattern after electroburning is the recrystallisation of the constriction,⁴⁵ which may lead to a higher
13 mean free path that is required for reflections on the μm scale. The interplay between reduced width
14 and reduced carrier density may also increase the factor λ/W , where $\lambda = hv_F/E$ is the wavelength of
15 the electrons. If this ratio becomes $\gtrsim 3 - 5$ the Fabry-Pérot interferences have a high contrast.¹¹
16
17
18
19
20
21
22
23

24
25 We now turn to the sharp anti-resonances in the interference regime as shown in Figure 3a and b
26 (around $V_g = -18$ V) in some samples (see Supplementary Information for data of other samples). The
27 slope of this anti-resonance feature is different from the slopes of the multi-mode FP interference
28 patterns. Repeated thermal cycling from 4 K to room temperature did not change the slope and
29 position of the feature observed at 4K (see Figure S8). The feature consists of an anti-
30 resonance/resonance double-peak as shown in Figure 3c. This asymmetric curve has a distinct Fano
31 line shape,⁴⁶ which is the result of coherent interaction between a localised resonant state with a
32 delocalised background state.¹ Fano resonances have previously been observed in double donor
33 systems in nanoscale silicon transistors⁴⁷ and in bundles of single walled CNTs⁴⁸. Fano resonances are
34 also predicted for single molecule systems, where a backbone state is coupled to the leads and a
35 pendant side-group is only coupled to the backbone but not to the leads.¹ In a graphene constriction
36 connected to mesoscopic graphene leads there are delocalised states that give rise to the previously
37 discussed FP pattern, and bound states e.g. localised along the edges due to edge roughness, that give
38 rise to Coulomb blockade at high positive gate voltages close to the Dirac point (see Figure 2f).³¹ We
39 attribute the observed Fano resonances to the coherent interaction between these states.
40
41
42
43
44
45
46
47
48
49
50
51
52
53
54
55
56
57
58
59
60

To estimate the coherent coupling strength between the localised and delocalised states in the graphene nanoconstriction, we fit the low bias current – gate voltage ($I - V_g$) traces to the Fano formula:^{48, 49}

$$G(\varepsilon) = G_{\text{non}} + G_{\text{res}} \frac{(\varepsilon + q)^2}{\varepsilon^2 + 1}, \quad (1)$$

where G_{res} is the coherent contribution to the conductance, q is the complex Fano factor,⁵⁰ $\varepsilon = 2(E - \varepsilon_s)/\Gamma_{\text{Fano}}$, ε_s and Γ_{Fano} are the energy and coupling strength of the resonant localised state and G_{non} is the conductance of the non-resonant channel. We model the non-resonant background as the sum of a constant offset G_{off} and a Breit-Wigner peak $A \frac{\Gamma^2}{\Gamma^2 + (E - \varepsilon_b)^2}$. This non-resonant background accounts for the conductance peak close to the observed anti-resonance feature. Fits to our data at different bias voltages using Equation (1) are shown as solid lines in Figure 3c. We find for a low bias of $V_b = 0.1$ mV: $\varepsilon_s = -18.3$ meV, $\text{Re}(q) = 0.3$, $\text{Im}(q) = 1.1$, $|q| = 1.1$, $\Gamma_{\text{Fano}} = 0.4$ meV, and a Breit-Wigner peak at $\varepsilon_b = -20.5$ meV with a coupling strength of $\Gamma = 1.1$ meV using a lever arm dE/dV_g of 1 meV/V extracted from the slope of the Fabry-Pérot interference pattern as depicted by the dotted black line in Figure 3a. The Fano factor q is a combined measure for the energetic detuning and the ratio of the transmission amplitudes of the resonant and the non-resonant channel.⁴⁹ For $q \rightarrow \infty$, the transport is dominated by the resonant channel and the line shape becomes that of a Breit-Wigner peak. For $q \rightarrow 0$ non-resonant transport dominates resulting in a symmetric dip in the conductance.⁴⁹ The value of $|q| = 1.1$ found in our experiments results in an asymmetric feature with characteristic Fano line-shape.⁴⁸ The width of $\Gamma_{\text{Fano}} = 0.4$ meV of the resonant state is similar to the values of 0.25 – 0.5 meV found for carbon nanotube bundles.⁴⁸ The Fano factor q decreases with increasing positive bias voltage (see inset in Figure 3c) which we attribute to a detuning of the energies of the localised state and the extended states. For large negative bias voltages the detuning changes the Fano factor from 1 to a high value, and the transport is dominated by a resonant channel resulting in a Breit-Wigner peak. The slope of the Fano feature, as seen in Figure 3a, results from the electrostatic coupling of the localised ‘pendant’ state to the gate and lead electrodes. Figure 4a, shows a tight-binding model of a pendant state interacting with an extended ‘backbone’ state. A chain of 5 sites acts as the backbone,

1
2
3 while a single site coupled to the second site of the backbone serves as pendant group. Figure 4b
4 shows the calculated transmission coefficient $T(E)$ as a function of energy E . A Fano-resonance
5 appears at an energy of about 0.5 eV, which is associated with the site energy of the bound state. The
6 various transmission maxima are Fabry-Pérot resonances of the backbone channel. To calculate the
7 differential conductance characteristic $dI/dV_b(V_b, V_g)$ of the device for different gate voltages V_g , bias
8 and gate voltage dependent transmission coefficients $T(E, V_b, V_g)$ were calculated for two different
9 potential profiles, where i) the bias drops over the left and right contacts (Figure 4c); or ii) the bias
10 drops along the device channel (Figure 4d). In the case where the bias voltage drops across the
11 contacts (see Figure 4c), the on-site energies of the pendant group and the backbone are not
12 influenced by the applied bias voltage. As a consequence the two anti-resonance Fano lines have the
13 same slope as the Fabry-Pérot interference lines (see Figure 4e). In contrast, when the potential drops
14 over the channel (see Figure 4d), the slopes of the anti-resonance lines and the backbone resonances
15 become different (see Figure 4f). As a result of the asymmetry of the junction, one of the Fano lines
16 almost vanishes (see section S7 in the Supplementary Information for details). Comparing the
17 calculations in Figure 4e and f with the experimental data in Figure 3a, we can conclude that, firstly,
18 the investigated junctions are asymmetric and, secondly, that a considerable portion of the applied
19 voltage has to drop across the junction. In a more realistic model, where two hexagonal lattices are
20 connected to various scattering regions with and without pendant groups (see Figure 5), Fano
21 resonances can be only observed in junctions with pendant groups (see section S6 and S8 for more
22 details). Molecular-dynamics simulations and density functional theory calculations of different
23 atomic configurations during nanogap formation¹² further show that dangling carbon atoms and edge
24 disorder can lead to Fano resonance in the transmission spectra of partially burned graphene nanogaps
25 (see section S8 in the Supplementary Information).
26
27
28
29
30
31
32
33
34
35
36
37
38
39
40
41
42
43
44
45
46
47
48
49

50 In summary we investigated graphene nanoconstrictions fabricated by narrowing down bowtie shaped
51 graphene ribbons using a feedback controlled electroburning technique. In the case of weakly-coupled
52 constrictions, the transport is dominated by Coulomb blockade with addition energies up to 800 meV.
53 In the strongly coupled regime, we observe quasi-periodic chess board like pattern in the conductance
54
55
56
57
58
59
60

1
2
3 maps which we attribute to multi-mode Fabry-Pérot interferences of delocalised states whose length
4 scale agrees with two possible resonance conditions: reflections inside the current-annealed low-
5 doped part of the device or reflections between the electrical contacts and the low-doped part. In some
6 of the devices, we observe sharp anti-resonances features with a Fano line shape inside the
7 interference regime in agreement with our tight binding modelling. We attribute these features to
8 interferences between the extended states and localised states inside the constriction. Such sharp anti-
9 resonances have the potential to underpin the development of low-power switches, because the
10 transmission of the structure can be tuned by a small gate voltage. Moreover, the Mott formula
11 predicts that a high $d\ln G/dV_g$ should also result in a high Seebeck coefficient⁵¹, making such devices
12 promising candidates for thermoelectric energy harvesting.
13
14
15
16
17
18
19
20
21
22
23
24
25
26

27 **Acknowledgements**

28
29 We thank the Royal Society for a Newton International Fellowship for J. A. M., the Agency for
30 Science Technology and Research (A*STAR) for a studentship for C.S.L. and a University Research
31 Fellowship for J. H. W. This work is supported by Oxford Martin School, the European Commission
32 (EC) FP7 ITN “MOLESCO” (project no. 606728) and UK EPSRC (grant nos. EP/K001507/1,
33 EP/J014753/1, EP/H035818/1 and EP/J015067/1). This project/publication was made possible
34 through the support of a grant from Templeton World Charity Foundation. The opinions expressed in
35 this publication are those of the author(s) and do not necessarily reflect the views of Templeton World
36 Charity Foundation. The authors would like to thank D. Gunlycke for his help and the useful
37 discussions and Y. Fan and J. Nägele for providing supporting transport data.
38
39
40
41
42
43
44
45
46
47
48
49
50

51 **Supporting Information**

52
53 Supporting SEM images of the devices, Electrical characterization of graphene used in this study,
54 Supporting micro Raman data, detailed study of interference pattern, additional Fano data, bias
55 dependence of the Fano feature, molecular-dynamics simulations.
56
57
58
59
60

Corresponding Author

*E-mail: <mailto:pascal.gehring@materials.ox.ac.uk>

References

1. Lambert, C. J. *Chem. Soc. Rev.* **2015**, *44*, 875-888.
2. Finch, C. M.; Garcia-Suarez, V. M.; Lambert, C. J. *Phys. Rev. B* **2009**, *79*, 033405.
3. Rong, Y. M.; Warner, J. H. *ACS Nano* **2014**, *8*, 11907-11912.
4. Chuvilin, A.; Meyer, J. C.; Algara-Siller, G.; Kaiser, U. *New J. Phys.* **2009**, *11*, 083019.
5. Son, Y. W.; Cohen, M. L.; Louie, S. G. *Nature* **2006**, *444*, 347-349.
6. Pezoldt, J.; Hummel, C.; Hanisch, A.; Hotovy, I.; Kadlecikova, M.; Schwierz, F. *Phys. Status Solidi C* **2010**, *7*, 390-393.
7. Mol, J. A.; Lau, C. S.; Lewis, W. J. M.; Sadeghi, H.; Roche, C.; Cnossen, A.; Warner, J. H.; Lambert, C. J.; Anderson, H. L.; Briggs, G. A. D. *Nanoscale* **2015**, *7*, 13181-13185.
8. Sadeghi, H.; Sangtarash, S.; Lambert, C. J. *Beilstein J. Nanotechnol.* **2015**, *6*, 1413-1420.
9. Candini, A.; Klyatskaya, S.; Ruben, M.; Wernsdorfer, W.; Affronte, M. *Nano Lett.* **2011**, *11*, 2634-2639.
10. Lu, Y.; Goldsmith, B.; Strachan, D. R.; Lim, J. H.; Luo, Z. T.; Johnson, A. T. C. *Small* **2010**, *6*, 2748-2754.
11. Darancet, P.; Olevano, V.; Mayou, D. *Phys. Rev. Lett.* **2009**, *102*, 136803.
12. Sadeghi, H.; Mol, J. A.; Lau, C. S.; Briggs, G. A. D.; Warner, J.; Lambert, C. J. *Proc. Natl. Acad. Sci. U. S. A.* **2015**, *112*, 2658-2663.
13. Ihn, T.; Guttinger, J.; Molitor, F.; Schnez, S.; Schurtenberger, E.; Jacobsen, A.; Hellmuller, S.; Frey, T.; Droscher, S.; Stampfer, C.; Ensslin, K. *Mater. Today* **2010**, *13*, 44-50.
14. Allen, M. T.; Martin, J.; Yacoby, A. *Nat. Commun.* **2012**, *3*, 934.
15. Moser, J.; Bachtold, A. *Appl. Phys. Lett.* **2009**, *95*, 173506.

- 1
2
3 16. Ki, D. K.; Morpurgo, A. F. *Phys. Rev. Lett.* **2012**, *108*, 266601.
4
5 17. Barreiro, A.; van der Zant, H. S. J.; Vandersypen, L. M. K. *Nano Lett.* **2012**, *12*, 6096-6100.
6
7 18. Lau, C. S.; Mol, J. A.; Warner, J. H.; Briggs, G. A. D. *Phys. Chem. Chem. Phys.* **2014**, *16*,
8
9 20398-20401.
10
11 19. Wu, Y. M. A.; Fan, Y.; Speller, S.; Creeth, G. L.; Sadowski, J. T.; He, K.; Robertson, A. W.;
12
13 Allen, C. S.; Warner, J. H. *ACS Nano* **2012**, *6*, 5010-5017.
14
15 20. Sun, Z. Z.; Yan, Z.; Yao, J.; Beitler, E.; Zhu, Y.; Tour, J. M. *Nature* **2010**, *468*, 549-552.
16
17 21. Ferrari, A. C.; Basko, D. M. *Nat. Nanotechnol.* **2013**, *8*, 235-246.
18
19 22. Puczkarski, P.; Gehring, P.; Lau, C. S.; Liu, J. J.; Ardavan, A.; Warner, J. H.; Briggs, G. A.
20
21 D.; Mol, J. A. *Appl. Phys. Lett.* **2015**, *107*, 133105.
22
23 23. Simmons, J. G. *J. Appl. Phys.* **1963**, *34*, 1793-1803.
24
25 24. Lau, C. S.; Sadeghi, H.; Rogers, G.; Sangtarash, S.; Dallas, P.; Porfyakis, K.; Warner, J.;
26
27 Lambert, C. J.; Briggs, G. A. D.; Mol, J. A. *Nano Lett.* **2016**, *16*, 170-176.
28
29 25. Burzurí, E.; Island, J. O.; Díaz-Torres, R.; Fursina, A.; González-Campo, A.; Roubeau, O.;
30
31 Teat, S. J.; Aliaga-Alcalde, N.; Ruiz, E.; van der Zant, H. S. J. *ACS Nano* **2016**, *10*, 2521-2527.
32
33 26. Hanson, R.; Kouwenhoven, L. P.; Petta, J. R.; Tarucha, S.; Vandersypen, L. M. K. *Rev. Mod.*
34
35 *Phys.* **2007**, *79*, 1217-1265.
36
37 27. Bischoff, D.; Varlet, A.; Simonet, P.; Eich, M.; Overweg, H. C.; Ihn, T.; Ensslin, K. *Appl.*
38
39 *Phys. Rev.* **2015**, *2*, 031301.
40
41 28. Muñoz-Rojas, F.; Jacob, D.; Fernández-Rossier, J.; Palacios, J. J. *Phys. Rev. B* **2006**, *74*,
42
43 195417.
44
45 29. Miao, F.; Wijeratne, S.; Zhang, Y.; Coskun, U. C.; Bao, W.; Lau, C. N. *Science* **2007**, *317*,
46
47 1530-1533.
48
49 30. Oksanen, M.; Uppstu, A.; Laitinen, A.; Cox, D. J.; Craciun, M. F.; Russo, S.; Harju, A.;
50
51 Hakonen, P. *Phys. Rev. B* **2014**, *89*, 121414.
52
53 31. Bischoff, D.; Libisch, F.; Burgdorfer, J.; Ihn, T.; Ensslin, K. *Phys. Rev. B* **2014**, *90*, 115405.
54
55 32. Rickhaus, P.; Maurand, R.; Liu, M. H.; Weiss, M.; Richter, K.; Schonenberger, C. *Nat.*
56
57 *Commun.* **2013**, *4*, 2342.
58
59
60

- 1
2
3 33. Gunlycke, D.; White, C. T. *Appl. Phys. Lett.* **2008**, *93*, 122106.
4
5 34. Kretinin, A. V.; Popovitz-Biro, R.; Mahalu, D.; Shtrikman, H. *Nano Lett.* **2010**, *10*, 3439-
6 3445.
7
8 35. Liang, W. J.; Bockrath, M.; Bozovic, D.; Hafner, J. H.; Tinkham, M.; Park, H. *Nature* **2001**,
9 *411*, 665-669.
10
11 36. Morozov, S. V.; Novoselov, K. S.; Katsnelson, M. I.; Schedin, F.; Ponomarenko, L. A.; Jiang,
12 D.; Geim, A. K. *Phys. Rev. Lett.* **2006**, *97*, 016801.
13
14 37. Staley, N. E.; Puls, C. P.; Liu, Y. *Phys. Rev. B* **2008**, *77*, 155429.
15
16 38. Berger, C.; Song, Z. M.; Li, X. B.; Wu, X. S.; Brown, N.; Naud, C.; Mayou, D.; Li, T. B.;
17 Hass, J.; Marchenkov, A. N.; Conrad, E. H.; First, P. N.; de Heer, W. A. *Science* **2006**, *312*, 1191-
18 1196.
19
20 39. Hwang, C.; Siegel, D. A.; Mo, S. K.; Regan, W.; Ismach, A.; Zhang, Y. G.; Zettl, A.;
21 Lanzara, A. *Sci. Rep.* **2012**, *2*, 590.
22
23 40. Lee, G. H.; Jeong, D.; Choi, J. H.; Doh, Y. J.; Lee, H. J. *Phys. Rev. Lett.* **2011**, *107*, 146605.
24
25 41. Lara-Avila, S.; Tzalenchuk, A.; Kubatkin, S.; Yakimova, R.; Janssen, T. J. B. M.; Cedergren,
26 K.; Bergsten, T.; Fal'ko, V. *Phys. Rev. Lett.* **2011**, *107*, 166602.
27
28 42. Baker, A. M. R.; Alexander-Webber, J. A.; Altebaeumer, T.; Janssen, T. J. B. M.;
29 Tzalenchuk, A.; Lara-Avila, S.; Kubatkin, S.; Yakimova, R.; Lin, C. T.; Li, L. J.; Nicholas, R. J. *Phys.*
30 *Rev. B* **2012**, *86*, 235441.
31
32 43. Ryu, S.; Liu, L.; Berciaud, S.; Yu, Y. J.; Liu, H. T.; Kim, P.; Flynn, G. W.; Brus, L. E. *Nano*
33 *Lett.* **2010**, *10*, 4944-4951.
34
35 44. Cheianov, V. V.; Fal'ko, V. I. *Phys. Rev. B* **2006**, *74*, 041403.
36
37 45. Qi, Z. J.; Daniels, C.; Hong, S. J.; Park, Y. W.; Meunier, V.; Drndic, M.; Johnson, A. T. C.
38 *ACS Nano* **2015**, *9*, 3510-3520.
39
40 46. Miroshnichenko, A. E.; Flach, S.; Kivshar, Y. S. *Rev. Mod. Phys.* **2010**, *82*, 2257-2298.
41
42 47. Verduijn, J.; Tettamanzi, G. C.; Lansbergen, G. P.; Collaert, N.; Biesemans, S.; Rogge, S.
43 *Appl. Phys. Lett.* **2010**, *96*, 072110.
44
45 48. Babić, B.; Schönenberger, C. *Phys. Rev. B* **2004**, *70*, 195408.
46
47
48
49
50
51
52
53
54
55
56
57
58
59
60

- 1
2
3 49. Gores, J.; Goldhaber-Gordon, D.; Heemeyer, S.; Kastner, M. A.; Shtrikman, H.; Mahalu, D.;
4
5 Meirav, U. *Phys. Rev. B* **2000**, *62*, 2188-2194.
6
7 50. Clerk, A. A.; Waintal, X.; Brouwer, P. W. *Phys. Rev. Lett.* **2001**, *86*, 4636-4639.
8
9 51. Cutler, M.; Mott, N. F. *Phys. Rev.* **1969**, *181*, 1336-1340.
10
11
12
13
14
15
16
17
18
19
20
21
22
23
24
25
26
27
28
29
30
31
32
33
34
35
36
37
38
39
40
41
42
43
44
45
46
47
48
49
50
51
52
53
54
55
56
57
58
59
60

Captions

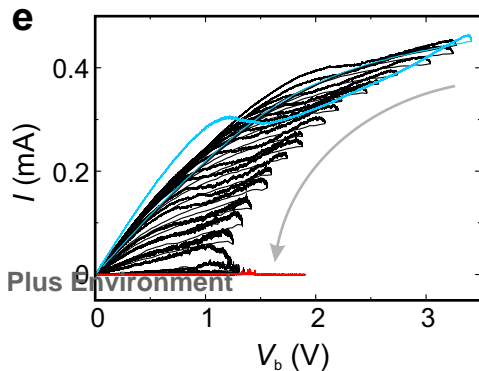
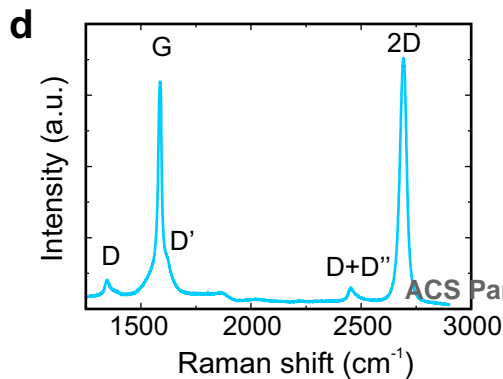
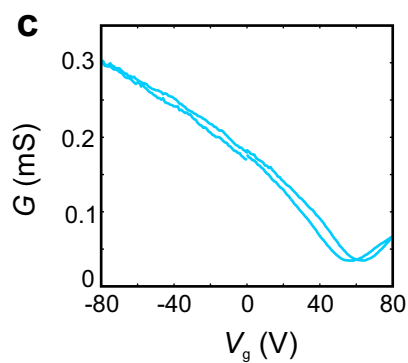
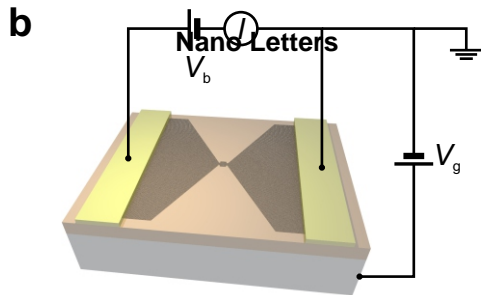
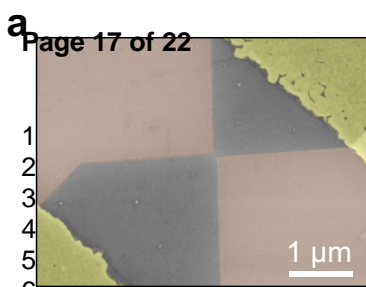
Figure 1. (a) False colour SEM image of a graphene constriction (grey) contacted by gold contacts (yellow). (b) Schematic of a graphene nanoconstriction device. (c) Conductance as a function of back gate voltage recorded at $V_b = 100$ mV of an as-prepared device. (d) Raman spectrum of the centre region of the graphene bow-tie after electroburning. (e) $I - V_b$ traces recorded during feedback-controlled electroburning. The first and last traces are shown in blue and red, respectively.

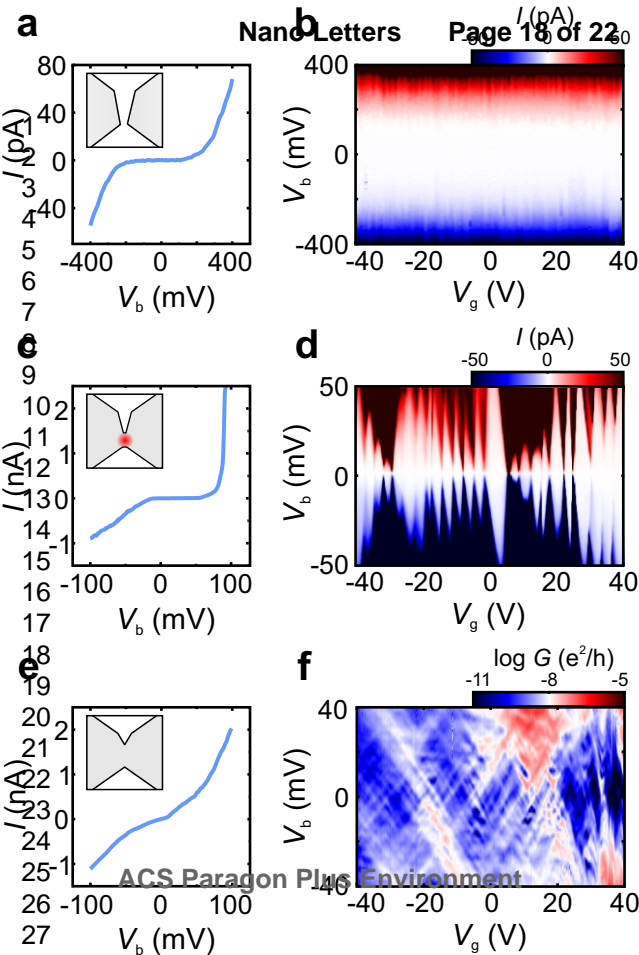
Figure 2. Nanostructures with different electronic behaviour formed during electroburning. (a) $I - V_b$ trace and (b) current map of an empty gap. (c) $I - V_b$ trace and (d) current map of a weakly coupled constriction showing sequential tunnelling. (e) $I - V_b$ trace and (f) conductance map of a strongly coupled constriction showing resonance effects. All data was recorded at $T = 4$ K under vacuum. The insets depict a scheme of the constriction.

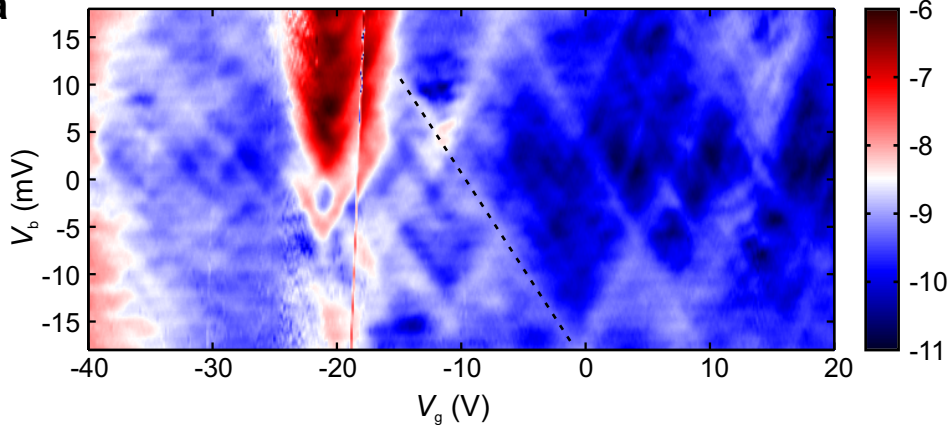
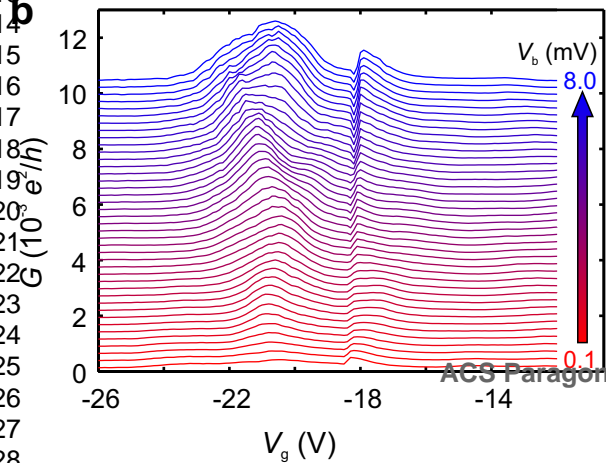
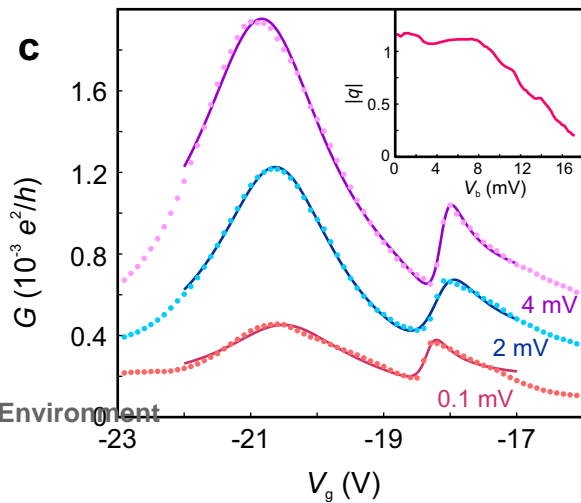
Figure 3. (a) Conductance map at $T = 4$ K of a strongly coupled constriction showing interference effects. A sharp anti-resonance feature around $V_g = -18$ V can be observed. The dotted line is used to extract the lever arm. (b) Gate traces for different bias voltages $0.1 \text{ mV} \leq V_b \leq 8 \text{ mV}$ in 0.2 mV steps of the data shown in (a). The curves are offset by $0.2 \times 10^3 e^2/h$ for clarity. (c) Gate traces at different bias voltages (dotted lines) and fits using Equation 1 (solid lines). The inset shows the dependence of the Fano factor $|q|$ as a function of the applied bias voltage.

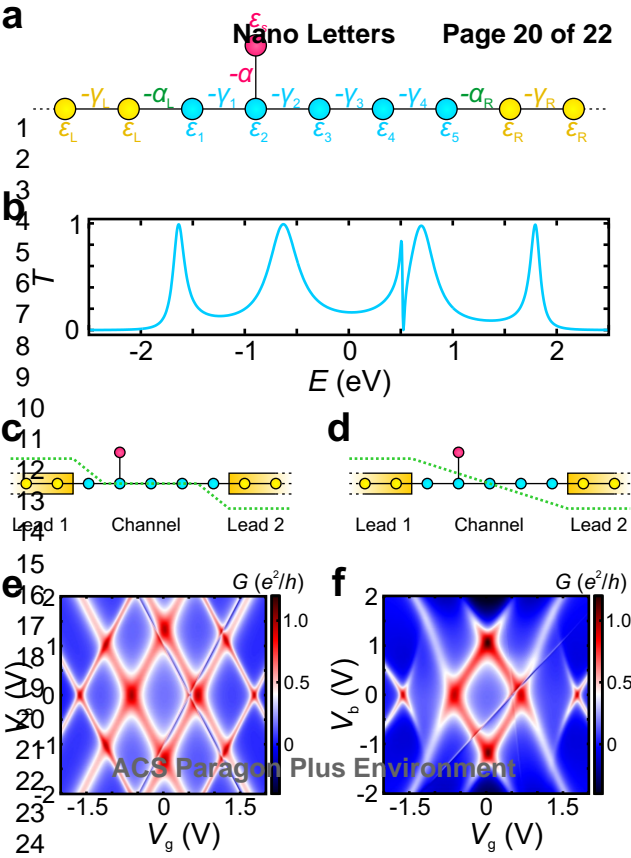
Figure 4. (a) Tight-binding model of a pendant state interacting with an extended 'backbone' state. The backbone is described by a chain of 5 sites with on-site energies ε_{1-5} that are coupled by hopping matrix elements $-\gamma_{1-4}$ and coupled to the leads via the outer most sites by hopping matrix elements $-\alpha_L$ (on the left side) and $-\beta_R$ (on the right side). The pendant group with an on-site energy ε_s is coupled to the second site of the backbone by a hopping matrix element $-\alpha$. (b) Calculated transmission coefficient as a function of energy. (c), (d) Sketch of the potential profile where (c) the bias drops over the left and right contacts and (d) the bias voltage drops along the device channel. (e), (f) Corresponding conductance maps as a function of bias and gate voltage for the cases depicted in (c), (d), respectively.

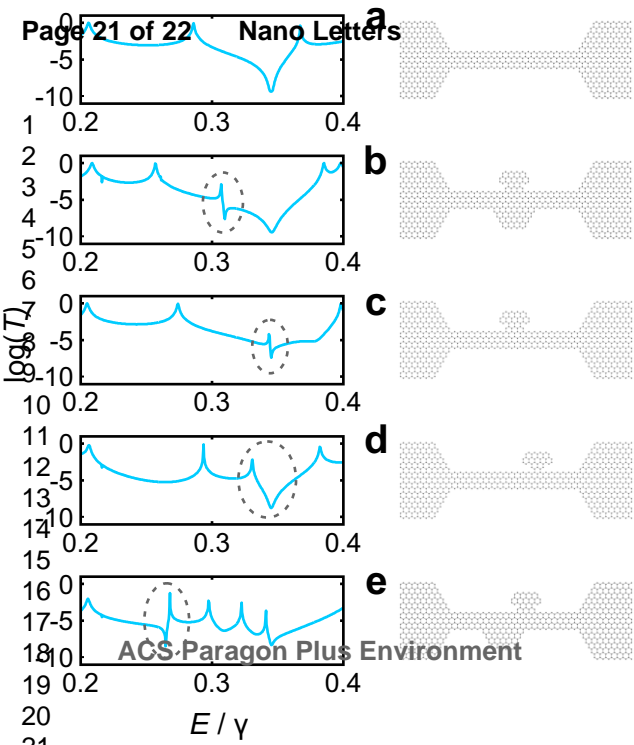
1
2
3 **Figure 5.** Transmission through graphene junctions. (a) Clean graphene ribbon connected to two
4 graphene electrodes, (b-e) graphene junctions with different shape and position of pendent groups.
5
6
7 The dotted circles indicate the position of Fano features.
8
9
10
11
12
13
14
15
16
17
18
19
20
21
22
23
24
25
26
27
28
29
30
31
32
33
34
35
36
37
38
39
40
41
42
43
44
45
46
47
48
49
50
51
52
53
54
55
56
57
58
59
60

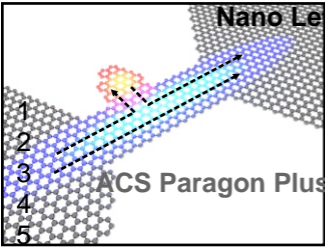




a**b****c**







Conductance

